Case Report

Forensic Analysis on Damage of a Cable-Stayed Bridge without Backstays Using BIM Information

Qi Xu, Xuefei Shi, Ziqi Xu * and Haiying Ma

Department of Bridge Engineering, Tongji University, Shanghai 200092, China; xuqi1913@tongji.edu.cn (Q.X.); shixf@tongji.edu.cn (X.S.); mahaiying@tongji.edu.cn (H.M.)
* Correspondence: xuziqi@tongji.edu.cn

Abstract: Serious cracks were found in the pylon of a cable-stayed bridge without backstays. Based on forensic damage investigation, this paper uses the finite element (FE) method incorporating Building Information Modeling (BIM) to analyze the causes of cracking. The BIM model is established based on the survey of design, construction, and service information of the bridge. Then, FE analysis is conducted using BIM information. Finally, the causes of cracking in different regions of the pylon are explained in detail. The results show that the FE simulation agrees well with the inspected distribution of cracks, and the causes of cracks are closely related to the pylon construction process. The main cause of the cracks is the shrinkage difference between concrete segments of different ages. The anchorage effect of stayed cables also causes inclined cracks perpendicular to the cable direction. The combination of temperature load and concrete shrinkage results in cracks at the root of the pylon, and the reduction in cable forces exacerbates the cracking.

Keywords: forensic analysis; cable-stayed bridge without backstays; crack; finite element modeling; BIM; concrete shrinkage

1. Introduction

A cable-stayed bridge without backstays is a modern novel bridge form that gives a sense of lightness and strength. This bridge type could realize a harmonious unification of function and aesthetics and has received wide engineering practice in recent years, especially in urban landscape environments [1]. Cable-stayed bridges without backstays began to appear when the Alamillo Bridge was built in 1992 to welcome the Sevilla Expo in Spain. The bridge was designed as a novel structure with a tilt pylon and single cable. When the bridge was completed, it became the landmark of Sevilla and a model for the world's bridges [2]. Though the structure of the bridge is not so efficient, the innovative appearance is undoubtedly an unusual example of cable-stayed bridges in the late 20th century [3]. Later, in 1998, the Mariinsky Bridge, built in the Czech Republic, was designed as a cable-stayed bridge without backstays and with a fan side. The bridge was selected as one of the top ten outstanding buildings of the International Engineering Association [4]. Since then, cable-stayed bridges without backstays have become more and more popular worldwide. A broad application of cable-stayed bridges without backstays was undertaken in China, such as the Changsha Hongshan Bridge, the Hefei Tongling Road Bridge, the Harbin Sun Island Bridge, and the Changchun Yitong River Bridge [5,6], and these bridges became unique landmarks.

In a cable-stayed bridge without backstays, the pylon can be regarded as a cantilever beam bearing forces of cables and self-weight, and the overturning moment of the pylon is entirely balanced by the forces of cables. Therefore, static analysis of this bridge form mainly focuses on the selection and consonance of girder weight, girder stiffness, pylon weight, pylon stiffness, and pylon–girder angle using the force equilibrium method [7]. Scholars and engineers have carried out theoretical analyses, numerical calculations, and experimental

studies on the design method and dynamic characteristics of cable-stayed bridges without backstays [5,8–11]. However, the mechanical behavior and force transmission path of cable-stayed bridges without backstays are quite different from those of conventional cable-stayed bridges. Complicated construction processes and environmental factors also lead to changes in the stress state of the bridge over time [12,13]. After years of operation, the bridge may present an unreasonable internal force state, resulting in potential hazards [14].

There are many factors affecting the occurrence and development of engineering structure diseases. Researchers have used forensic engineering to investigate the diseases and performance of structures by combining engineering principles with field investigations [15–17]. The application cases include the collapse and damage of buildings and bridges in the US [18–20], Italy [21–23], and Turkey [24,25]. These studies have identified the causes of structural disease or collapse and provided experience for future structural design, construction, operation, and maintenance.

The force state of cable-stayed bridges is closely dependent on the construction process. Incorporating the building information model (BIM), the whole-process finite-element (FE) software such as Ansys can clearly and accurately simulate the force state change process of bridges from constructed stage to current service condition. In fact, several studies have illustrated the advances of incorporating BIM and FE for bridge analysis. Park et al. proposed a Web- and database-supported visualization method that enables real-time information sharing of BIM to analyze bridge performance and display construction states [26]. Hu et al. combined BIM and FE to analyze and manage process conflicts and structural safety during construction [27]. Mcguire et al. presented a method using BIM software (Revit) to link and analyze inspection, evaluation, and management data of bridges [28]. Brando et al. used a forensic investigation modeling (similar to BIM) method to clearly present the causes of the collapse of the I-35W Bridge [20]. Kim et al. proposed a BIM-based quantitative evaluation framework, which incorporated buildings' physical and environmental characteristics to enhance fire safety performance [29]. Nathaniel et al. used BIM to integrate unmanned aerial vehicle imagery and building component identification and enabled component-level damage evaluation of building systems [30].

In this paper, a prestressed concrete cable-stayed bridge without backstays was studied to find the crack causes. The bridge has been in service for five years, and cracks in different regions were detected in the pylon. The cause of these cracks was attributed to the construction process and environmental conditions based on forensic engineer investigation. In order to illustrate the occurrence and development of these cracks, a further forensic analysis of the damage was conducted, where a BIM model was applied to address the complicated construction procedures and pylon geometry. Then, the FE model was established to simulate the stress conditions in critical regions of the structure. Based on BIM and FE analysis, the calculation results are consistent with the crack distribution found from the field investigation, and the cause of the cracks has been revealed. The research procedure is shown in Figure 1.
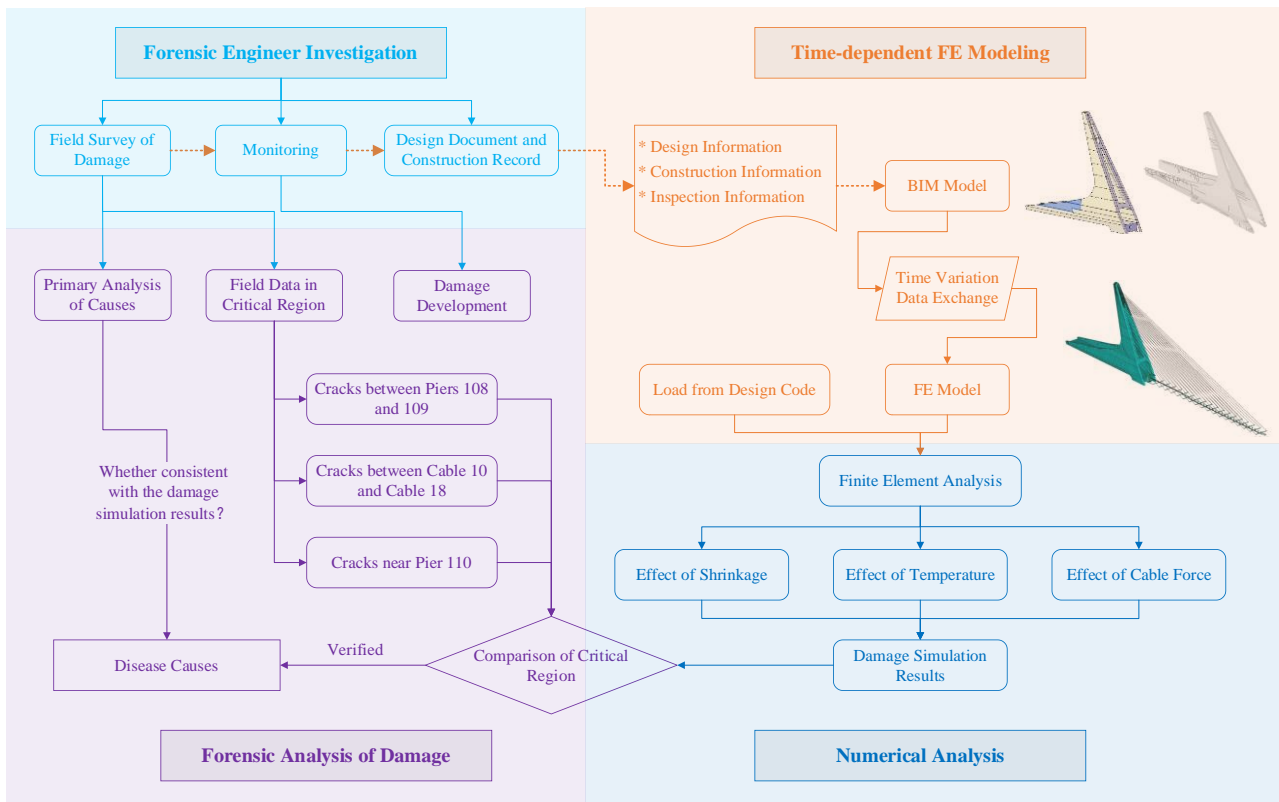
Figure 1. Analysis procedure.

2. Forensic Engineer Investigation

2.1. Design Document of the Bridge

The cable-stayed bridge without backstays was designed for a double-lane light city rail; the layout is shown in Figure 2. The span arrangement of the bridge is 30 m + 44 m + 130 m. The height of the single concrete pylon is 65 m, and the width of the prestressed concrete girder is 13 m. The pylon–girder angle is 58°, and 18 pairs of cables are connected with the pylon and the girder (See Figure 2a). The pylon consists of two walls with a thickness of 1.5 m, and the walls are placed on the sides of the girder. The bottom of the walls is connected to the box girder by transverse beams (See Figure 2b). The inclined pylon can balance a part of the cable forces by its self-weight, which forms a collaborative force system.
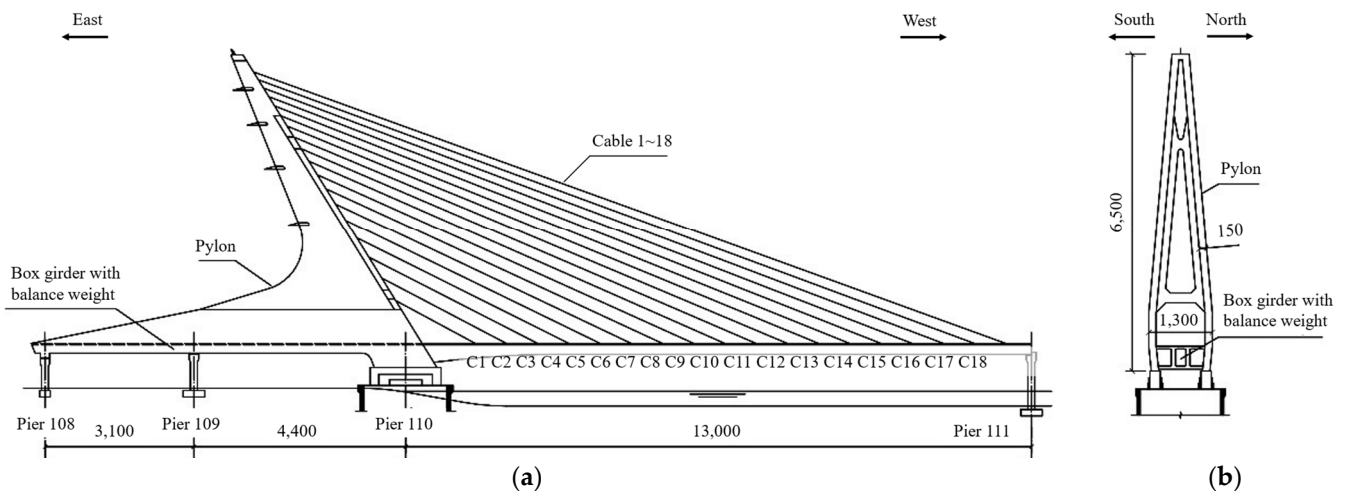

Figure 2. Layout of the bridge (units: cm): (**a**) elevation; (**b**) pylon section.

There are six vertical prestressed tendons (N1~N6) and six longitudinal prestressed tendons (N7~N12) in the pylon, as shown in Figure 3. These prestressed tendons are designed to balance the bending moment in the pylon induced by stayed cables.
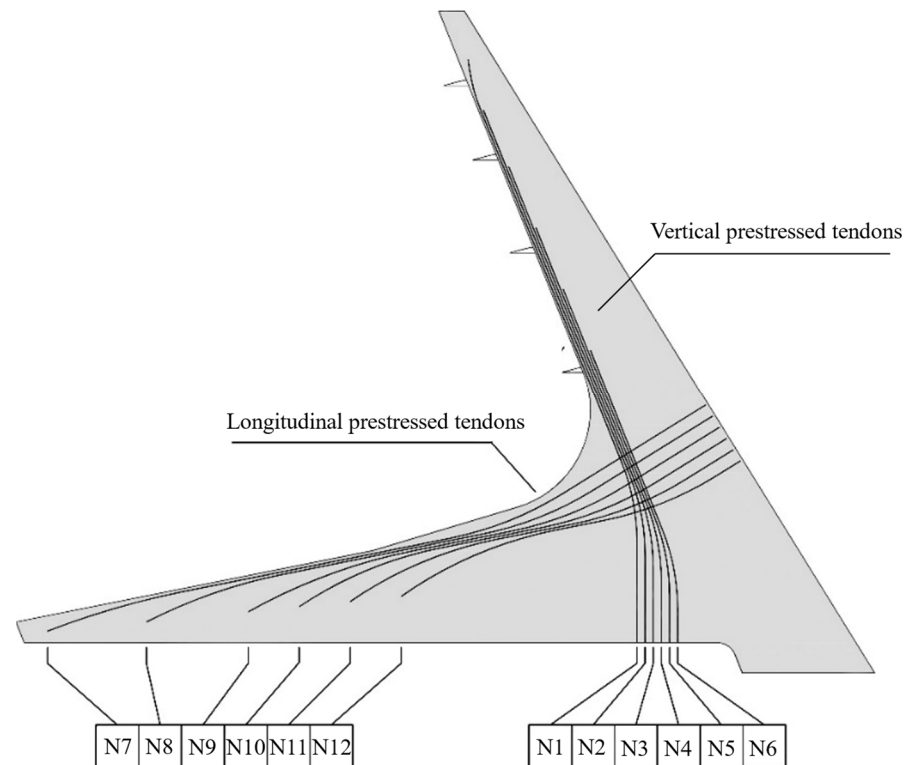

Vertical prestressed tendons

Longitudinal prestressed tendons

| N7 | N8 | N9 | N10 | N11 | N12 |

| N1 | N2 | N3 | N4 | N5 | N6 |

Figure 3. Profile of prestressed tendons in the pylon.

2.2. Construction Records

The girder and pylon were cast on site using full frame supports, as shown in Figure 4. The entire casting process of the pylon was finished with layer work. The box girder with balance weight was cast on 4 June and Segment 1 was cast on 6 August. Table 1 gives the casting information of the pylon. It took several months to finish the construction with significant temperature and humidity fluctuations. Additionally, there was an over four-month gap between the casting of the pylon and girder between Piers 108 and 109.

Table 1. The casting information of the pylon.

| Step	Content	Time	Volume (m³)	Concrete Slump (mm)	Temperature (°C)	Relative Humidity
1	Segment 1	2005/8/6	846	180	24.5	73%
2	Segment 2	2005/8/24	527	200	23.0	69%
3	Segment 3	2005/9/4	339	190	14.0	63%
4	Segment 4	2005/9/14	263	200	14.0	63%
5	Segment 5	2005/9/23	213	200	16.0	58%
6	Segment 6	2005/10/3	249	190	14.5	51%
7	Segment 7	2005/10/11	151	200	10.0	51%
8	The first part between Piers 108 and 109	2005/10/14	335	190	6.0	51%
9	The second part between Piers 108 and 109 in the south	2005/10/17	133	190	2.5	51%
10	Segment 8	2005/10/18	112	190	3.0	51%
11	Segment 9	2005/10/26	90	190	6.0	51%
12	The second part between Piers 108 and 109 in the north	2005/10/31	133	190	−2.0	51%
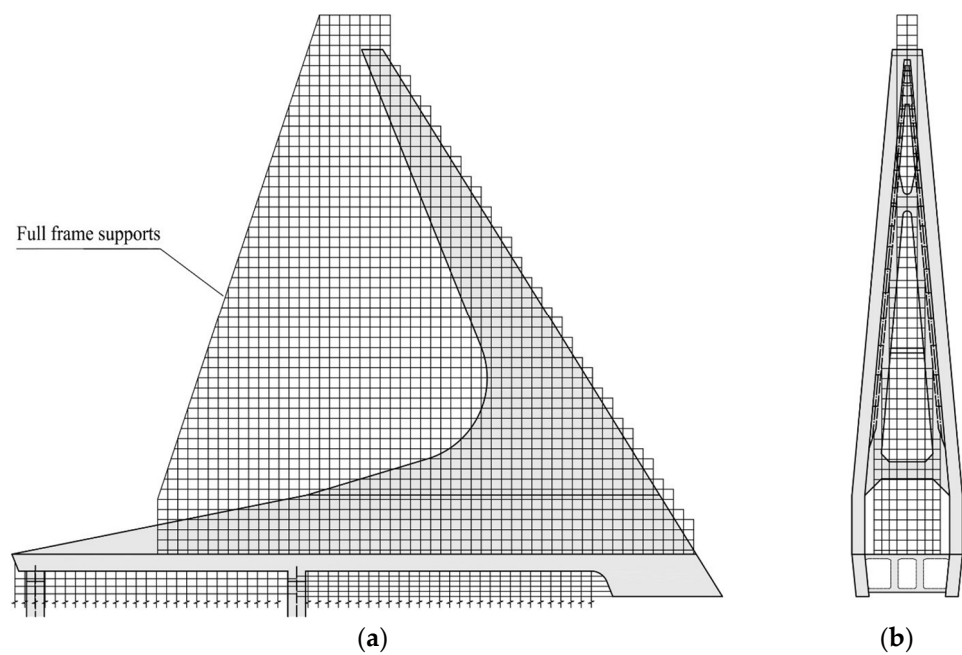
Figure 4. Layout of full frame supports during pylon construction: (**a**) elevation; (**b**) pylon section.

The tensile force for each prestressed tendon is 1707 t. The prestressed tendons in the pylon were stretched and anchored step by step along with the stretching procedure of the stayed cables.

2.3. Field Survey of Disease

2.3.1. Cracks

Severe cracks were detected in the pylon five years after the bridge was built. Figure 5 shows the distribution and detailed photographs of these cracks.
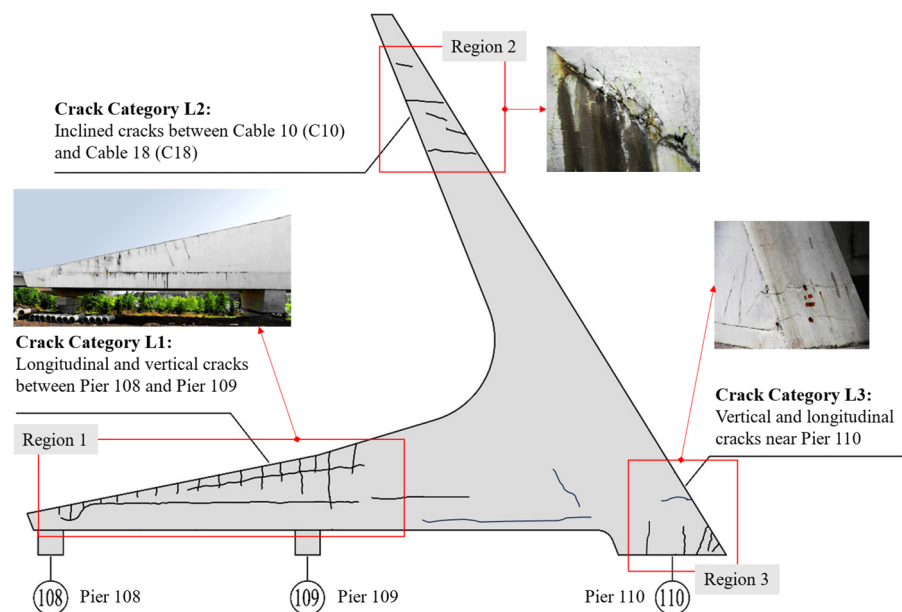

Figure 5. Distribution and detailed photographs of cracks in the pylon.

Cracks are classified into three categories according to their locations: (1) Crack Category L1: paralleled vertical and longitudinal cracks on the pylon wall between Piers 108 and 109 (Region 1 in Figure 5); (2) Crack Category L2: inclined cracks in the top

anchorage zone between cable 10 and cable 18 (Region 2 in Figure 5); (3) Crack Category L3: short vertical and longitudinal cracks at the bottom of the pylon near Pier 110 (Region 3 in Figure 5).

The length of the cracks varied from 0.5 to 30 m. Most of the crack widths ranged from 0.02 to 0.15 mm, and the crack depths ranged from 9 to 32 mm. These were all shallow surface cracks. The distributions and widths of the cracks were discovered to remain the same by another inspection one year later.

The bridge is located in a dry and cold district, and the construction process of the pylon lasted several seasons. Thus, the environmental condition during construction shows a large variation, which may be an important cause of these cracks.

2.3.2. Reduction in Prestressing Force

An obvious reduction in prestressing force of the stayed cables also occurred. Figure 6 shows a comparison between the measured and design force of the stayed cables. A large reduction in prestressing force can be found from cable 8 to cable 18. For example, the measured cable force of C13 to C17 is 20% smaller than the design force, and the measured cable force of C18 is 30% smaller than its design value.
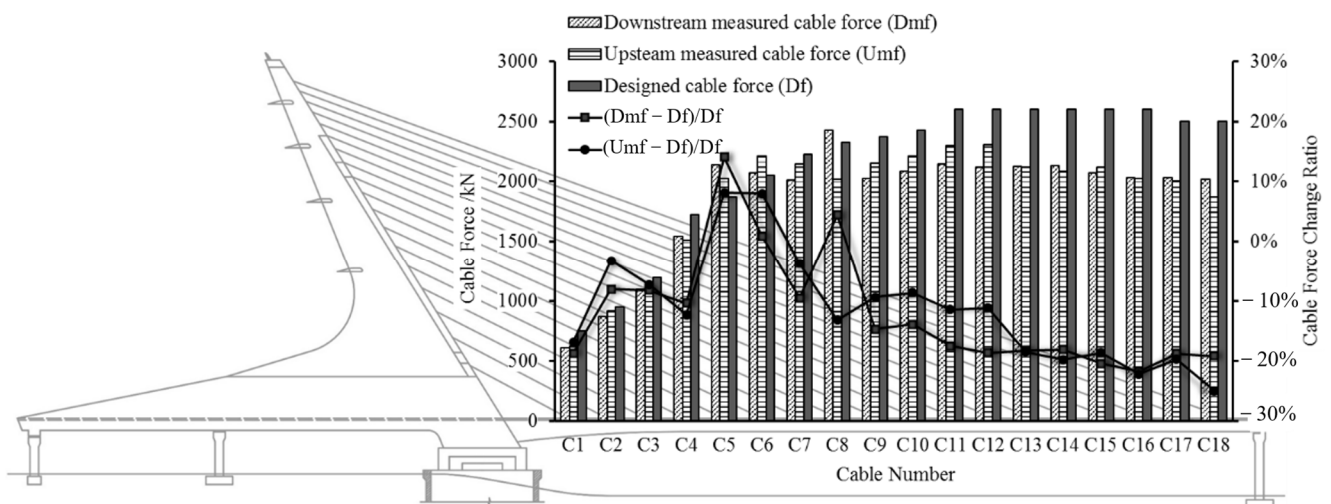

Figure 6. Comparison between measured and design force of stayed cables.

3. Time-Dependent FE Modeling

3.1. BIM Model

Due to the complicated geometry and construction process, as well as the tedious information on materials, environment, inspections, etc., it is difficult to perform the time-dependent FE analysis directly.

A BIM model was established, incorporating design, construction, and inspection information. First, a 3D model of the bridge is constructed based on the design drawing. Then, the construction process is recovered from the construction record, especially the information on different layers of the pylon, e.g., materials, environment, stretching force of prestressed tendons, and cable force at different times during the construction procedure. The casting information on the pylon is listed in Table 1.

Figure 7 shows the simulation of the construction process using BIM information. Figure 8 shows the construction information on a pylon segment. The BIM model has comprehensive information on bridge design, construction, and inspection, which can be used to update the information based on bridge service conditions.
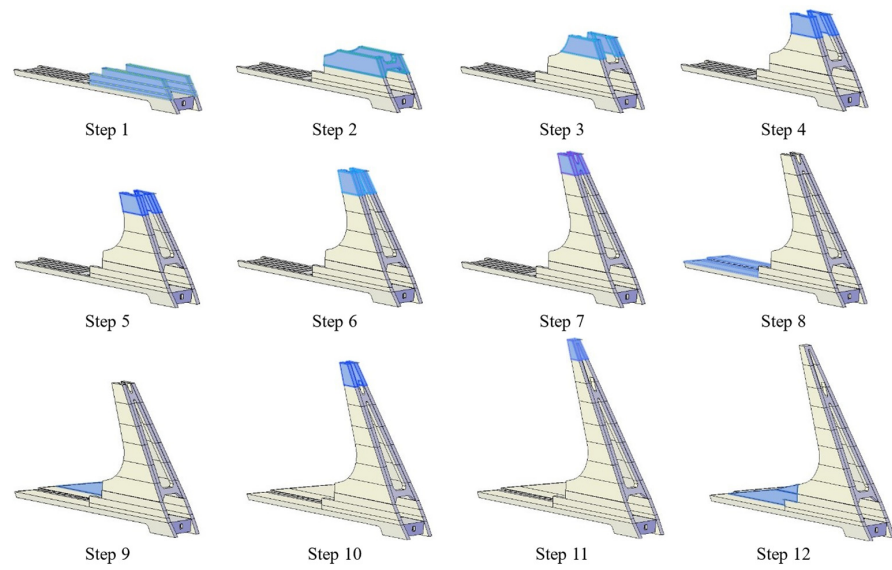
Figure 7. Simulation of construction process using BIM information.

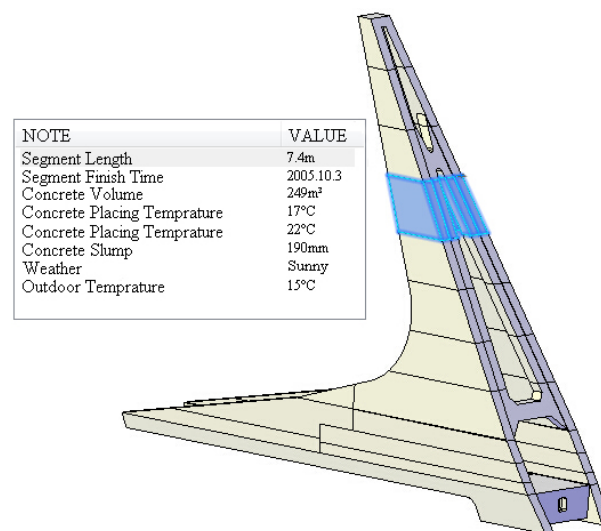| NOTE	VALUE
Segment Length	7.4m
Segment Finish Time	2005.10.3
Concrete Volume	249m³
Concrete Placing Temprature	17°C
Concrete Placing Temprature	22°C
Concrete Slump	190mm
Weather	Sunny
Outdoor Temprature	15°C

Figure 8. Construction information on a pylon segment.

Then, the FE model was accurately generated with the information conversion of BIM based on the roadmap in Figure 9.
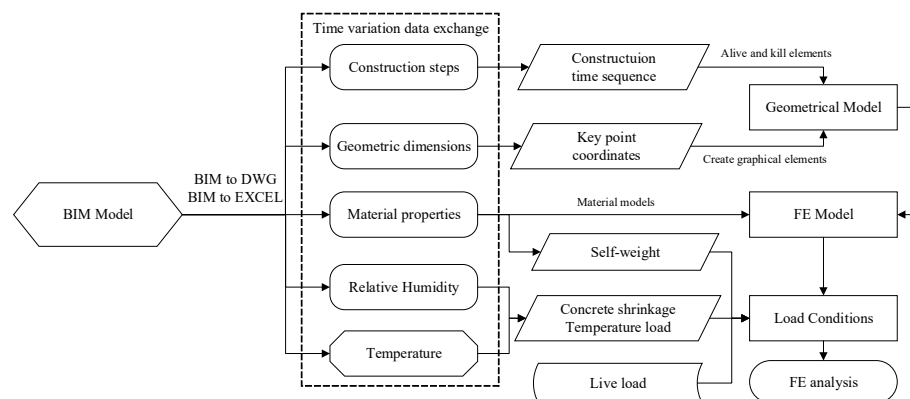

Figure 9. The roadmap for constructing the FE model using BIM information.

Firstly, the data in the BIM model was exported to DWG and EXCEL files, including the construction steps, geometric dimensions, material properties, relative humidity, and temperature. Secondly, the construction time sequence and key point coordinates of components were used to generate the geometric model. Thirdly, the material properties were used to determine material models, and the FE model was constructed. After that, the self-weight, concrete shrinkage, temperature load, and live load were calculated based on environmental data and traffic situation. Finally, finite element analysis was performed using different load conditions.

3.2. FE Model
3.2.1. Elements and Materials

Extracting the key points, geometry shape, and spatial coordinates directly from the BIM model, the parametric FE model is established in the ANSYS software based on APDL [31,32], as shown in Figure 10.
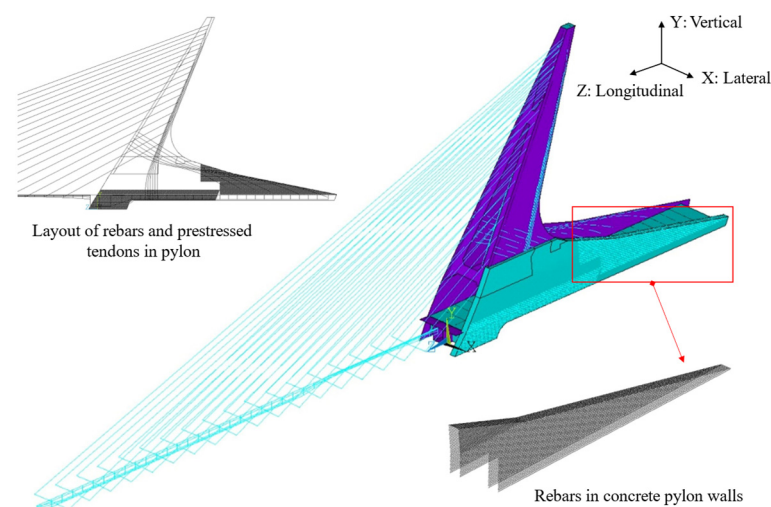

Figure 10. FE model.

To improve the calculation efficiency, the pylon is modeled by a combination of different elements. The main girders of the side span were simulated by Shell 281 elements, the main girders of the middle span were simulated by Beam 188 elements, and the stayed cables were simulated by Link 180 elements. In order to obtain more accurate calculation results, the cracking regions of the pylon were modeled using Solid 95 elements, and steel rebars were modeled using Link 180 elements to accurately simulate the effect of concrete shrinkage. The remaining parts of the pylon were modeled using Shell 281 elements.

Concrete compressive strength and tensile strength are set as 32.4 MPa and 2.65 MPa according to the standard value of material tests. The elastic modulus and Poisson's ratio of the concrete are set as 34,500 MPa and 0.2. The steel bars' elastic modulus is 2.06×10^5 MPa, and the yielding strength is 400 MPa. High-strength parallel steel wire ropes are used for stayed cables. The elastic modulus is 1.95×10^5 MPa, and the tensile strength is 1670 MPa. The density of the concrete is 2600 kg/m^3, and the density of the steel bars and stayed cables is 7850 kg/m^3.

3.2.2. Construction Process Simulation

According to Section 2.3.1, the cracks in this bridge were caused by the variable environmental conditions during construction and operation. To consider the effect of the construction process, the concrete casting process should be accurately simulated, which can be accomplished based on the construction process information obtained from the BIM model. The modeling of the construction process in the FE model is shown in Figure 11.
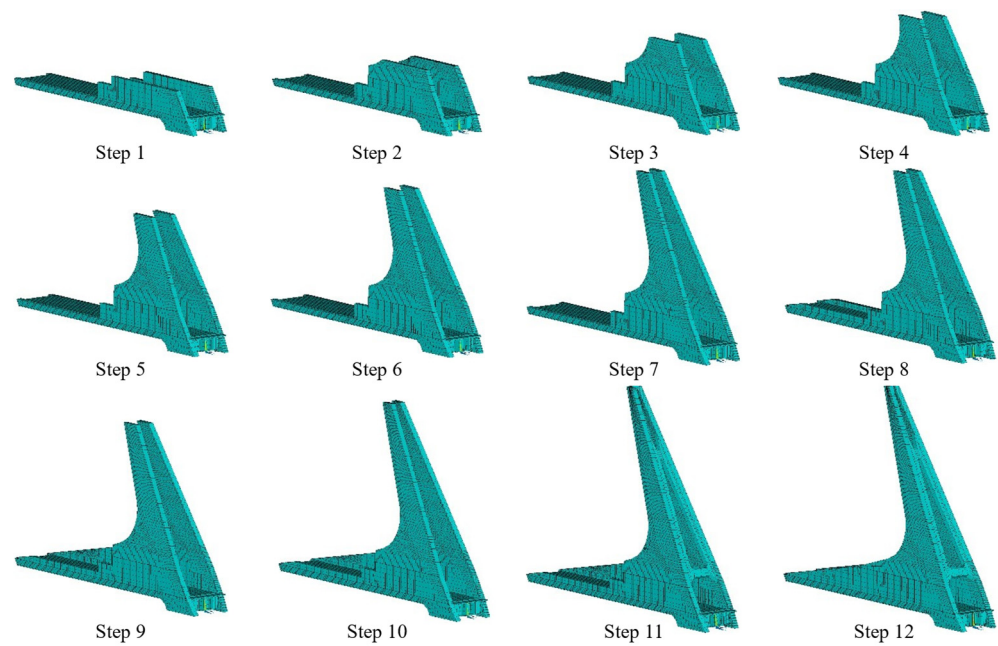
Figure 11. Modeling of construction process in FE model.

3.2.3. Concrete Shrinkage Simulation

To involve the effect of concrete shrinkage in the FE model, the shrinkage development curves were obtained based on the construction information of each pylon segment from the BIM model, e.g., casting volume, time, and humidity. The shrinkage of concrete is related to the age and thickness of the casting segment, the relative ambient humidity, etc. In the following equations, the effect of shrinkage was determined based on the equations defined in the Chinese bridge design standard (JTG 3362-2018) [33].

$$\varepsilon_{cs}(t, t_s) = \varepsilon_{cs0} \cdot \beta_s(t - t_s) \tag{1}$$

$$\varepsilon_{cs0} = \varepsilon_s(f_{cm}) \cdot \beta_{RH} \tag{2}$$

$$\varepsilon_s(f_{cm}) = \left[160 + 10\beta_{sc} \left(9 - \frac{f_{cm}}{f_{cm0}} \right) \right] \cdot 10^{-6} \tag{3}$$

$$\beta_{RH} = 1.55 \left[1 - \left(\frac{RH}{RH_0} \right)^3 \right] \tag{4}$$

$$\beta_s(t - t_s) = \left[\frac{(t - t_s)/t_1}{350(h/h_0)^2 + (t - t_s)/t_1} \right]^{0.5} \tag{5}$$

where t_s is the age of concrete when the shrinkage starts; t is the age of concrete at the time of calculation, which is determined by the casting time of each concrete segment; $\varepsilon_{cs}(t, t_s)$ is the shrinkage strain at the time of t; ε_{cs0} is the nominal shrinkage coefficient of concrete; f_{cm} is the average compressive strength of cubic concrete with curing time of 28 days; β_{RH} is a coefficient related to the annual average relative humidity; RH is the annual average ambient relative humidity; RH_0 = 100%; β_{sc} is a coefficient related to the cement type; $\beta_{sc} = 5.0$; h is the theoretical thickness of the concrete segment; h_0 = 100 mm; t_1 = 1 d.

Based on Equations (1)–(5), the shrinkage development curves for each concrete segment were determined, as shown in Figure 12. These curves were used to apply the effect of the concrete shrinkage to the FE model.
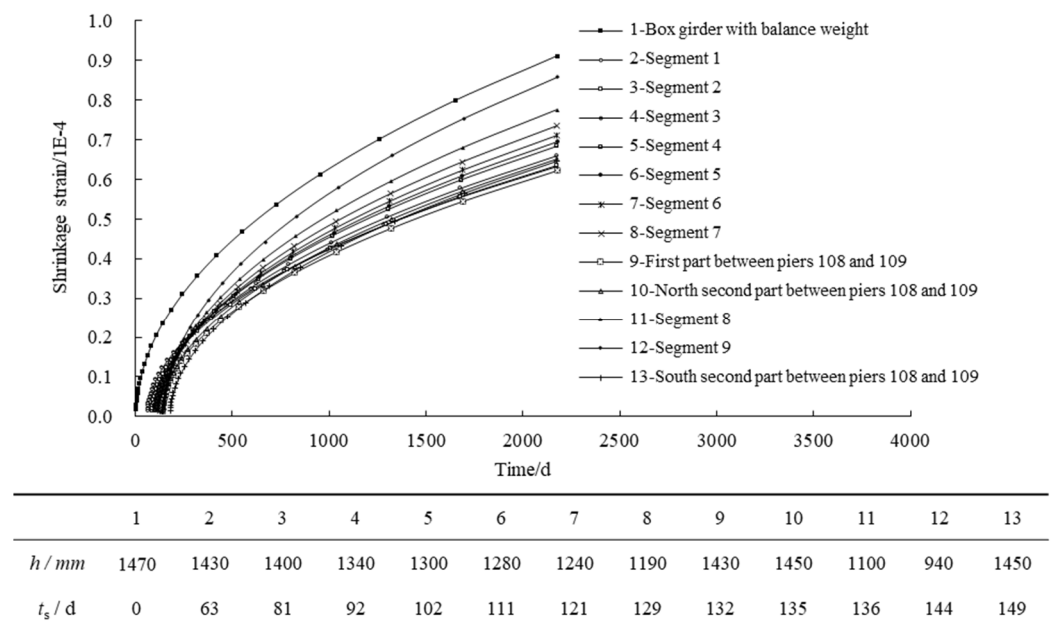
	1	2	3	4	5	6	7	8	9	10	11	12	13
h / mm	1470	1430	1400	1340	1300	1280	1240	1190	1430	1450	1100	940	1450
t_s / d	0	63	81	92	102	111	121	129	132	135	136	144	149

Figure 12. Curves of shrinkage strain for each concrete segment.

4. Numerical Analysis

4.1. Analysis Cases and Results

4.1.1. Analysis Cases and Load Conditions

In order to study the effect of the construction process, environmental conditions, and reduction in cable forces on the pylon's mechanical performance, several analysis cases of the bridge were carried out. The main loads were considered, including self-weight, temperature load, live load, and shrinkage. The deformations and stresses of the pylon and girder under different cases were calculated. The loading conditions for each case are shown in Table 2.

Table 2. Analysis cases and load conditions.

State	Cases	Cable Force	Load Conditions
Initial design	Case 1	Design cable force	Self-weight
	Case 2	Design cable force	Self-weight + Temperature load
	Case 3	Design cable force	Self-weight + Live load
Construction stage	Case 4	Measured cable force	Self-weight + Shrinkage
Service state	Case 5	Measured cable force	Self-weight
	Case 6	Measured cable force	Self-weight + Temperature load
	Case 7	Measured cable force	Self-weight + Live load

The maximum and minimum effective temperature standard values are 34 °C and −23 °C at the bridge location [34]. According to the construction records, the reference temperature at the completion of construction was −2 °C. As a result, the overall rising temperature of the bridge was 32 °C, and the overall falling temperature was −25 °C.

The bridge is located on a light rail line, and the load of light rail trains was mainly considered live load. According to the actual traffic situation, two light rail trains were loaded in the middle span at the same time, and the axle weight of the trains was 140 kN, as shown in Figure 13.
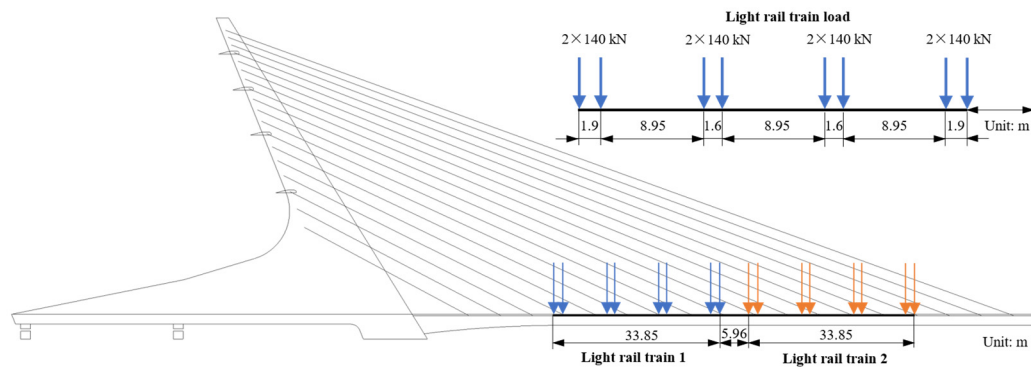
Figure 13. The value and unfavorable condition of live loads.

4.1.2. Analysis Results

Table 3 gives the stress (SY: vertical stress, SZ: longitudinal stress) ranges of Region 1 to 3 (see Figure 5) in each case, as well as the deformations (UY: vertical deformation, UZ: longitudinal deformation) of the box girder and pylon. The most unfavorable loading conditions are used for temperature load (overall falling temperature: −25 °C) and live load (see Figure 13) in Cases 2, 3, 6, and 7.

Table 3. Stress and deformation of critical regions in different cases.

Regions	Stress or Deformation	Case 1	Case 2	Case 3	Case 4	Case 5	Case 6	Case 7
Region 1	SY (MPa)	−3~1.5	−3~1.5	−2.5~1.5	−10~8	−1~2.5	−2.5~1.5	−3~2
	SZ (MPa)	−7~1	−7~1	−6.5~0.5	−4~8	−7~1	−7~0.5	−7~1
Region 2	SY (MPa)	−7~1	−7~1	−7~1	−4~6	−2~2.5	−2~2.5	−2~2.5
	SZ (MPa)	−3~0.5	−3~0.5	−3~0.5	−4~2	−1~1.5	−1~1.5	−1~1.5
Region 3	SY (MPa)	−7~1	−9~2	−8~1	−2~4	−8~2	−12~6	−8~1
	SZ (MPa)	−2~1	−2~6	−2~0.5	−2~4	−2~1.5	−4~8	−2~1
Box girder	UY (mm)	64 (↑ *)	74 (↑)	46 (↑)	−30 (↓)	−28 (↓)	−19 (↓)	−47 (↓)
Pylon top	UY (mm)	−7 (↓)	−33 (↓)	−6 (↓)	−10 (↓)	−10 (↓)	−36 (↓)	−9 (↓)
	UZ (mm)	8 (←)	26 (←)	8 (←)	−5 (→)	−3 (→)	21 (←)	2 (←)

* Arrows indicate the direction of displacement: ↑—upward, ↓—downward, ←—forward along the longitudinal direction of bridge, →—backward along the longitudinal direction of bridge.

Table 4 gives the variation in stress in the three regions at each construction step. The vertical tensile stress in Region 1 is generated at stage 1, and the tensile zone increases at stage 8; the longitudinal tensile stress occurs at stage 8. Vertical and longitudinal tensile stresses occur in Region 2 after the prestressing tendons and stayed cables tensioning at stage 13. Vertical and longitudinal tensile stress occur in Region 3 at stage 1 and increase at stage 8. At stage 14, the vertical and longitudinal tensile stress in both Region 1 and Region 3 increase after the long-term shrinkage effect, further indicating that the cracking in these two regions is related to concrete shrinkage.

Table 4. Stress state in Region 1 to 3 at each construction stage.

Construction Stage		Stresses in Region 1		Stresses in Region 2		Stresses in Region 3	
Stage	Construction Content	SY (MPa)	SZ (MPa)	SY (MPa)	SZ (MPa)	SY (MPa)	SZ (MPa)
1	Segment 1	+	-	/	/	+	+
2	Segment 2	+	-	/	/	+	+
3	Segment 3	+	-	/	/	+	+
4	Segment 4	+	-	/	/	+	+
5	Segment 5	+	-	/	/	+	+
6	Segment 6	+	-	/	/	+	+
7	Segment 7	+	-	/	/	+	+

Table 4. *Cont.*

Construction Stage		Stresses in Region 1		Stresses in Region 2		Stresses in Region 3	
Stage	Construction Content	SY (MPa)	SZ (MPa)	SY (MPa)	SZ (MPa)	SY (MPa)	SZ (MPa)
8	The first part between Piers 108 and 109	++	+	/	/	++	++
9	The second part between Piers 108 and 109 in the south	++	+	/	/	++	++
10	Segment 8	++	+	/	/	++	++
11	Segment 9	++	+	-	-	++	++
12	The second part between Piers 108 and 109 in the north	++	+	-	-	++	++
13	Pour main girder, tension stayed cables, and prestressing tendons	++	+	+	+	++	++
14	Long-term shrinkage simulation	+++	++	+	+	+++	+++

Note: "/" indicates the section has not been constructed; "-" indicates compressed stress; "+" indicates tensile stress; "++" and "+++" indicate an increase in tensile stress or tensile zone.

4.2. Effect of Concrete Shrinkage

According to the construction records of the pylon, the difference in concrete shrinkage strain generated by the age differences between pylon segments is one of the important effects. Figure 14 gives the concrete casting information between Piers 108 and 109. The age difference between the box girder and Segment 1 is 63 days, and the age difference between the box girder and the first part pylon wall between Piers 108 and 109 is 132 days.
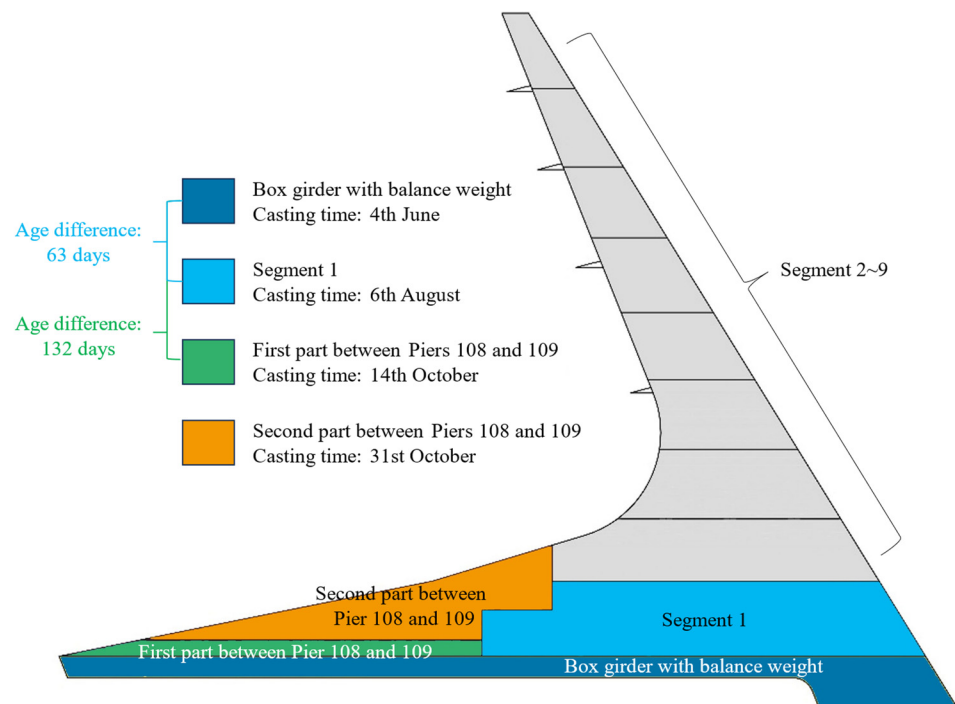

Figure 14. The concrete casting information between Piers 108 and 109.

Considering the structural self-weight and shrinkage effect at each construction stage, a simulation of the whole bridge construction process was carried out to analyze the stress distribution of the pylon. At stage 1, vertical tensile stress due to the shrinkage occurs along the longitudinal direction at the interface of the box girder and Segment 1, as shown in Figure 15. The shrinkage effect continues to develop with time, and the tensile stress in this region has not disappeared.
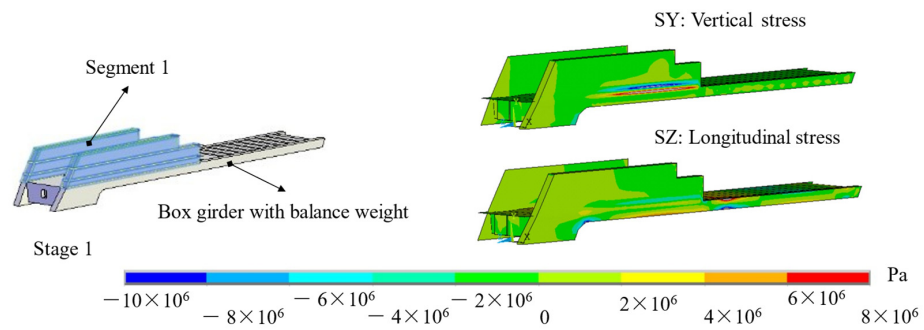
Figure 15. Stress distribution in pylon of construction stage 1.

From stage 8 to stage 12, the first and second parts of the pylon walls between Piers 108 and 109 were cast within half a month. However, the age difference between the box girder and the last-casting pylon wall is more than 4 months. As shown in Figure 16, large vertical tensile stress is generated at the interface of concrete, and large longitudinal tensile stress is generated at the upper free edge due to the restraining of the lower pylon wall.
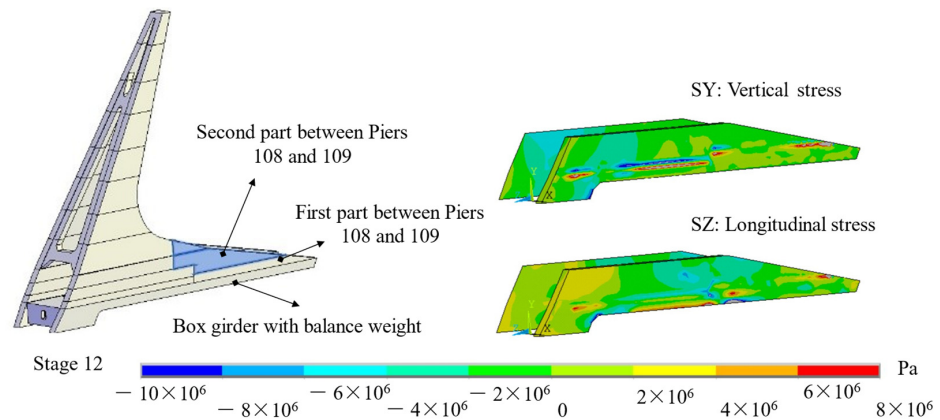

Figure 16. Stress distribution in pylon of construction stage 12.

The long-term shrinkage simulation was continued after the finish of the construction process simulation, and the vertical and longitudinal stress distribution of the pylon is shown in Figure 17.
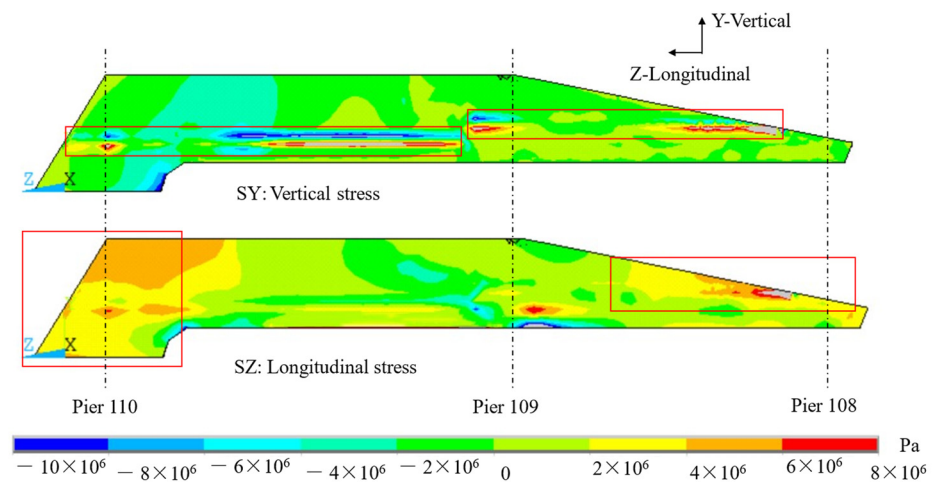

Figure 17. Stress distribution in pylon under long-term shrinkage.

At the interface of the old and new concrete layers, there is more than 6 MPa vertical tensile stress distributing along the pylon wall, resulting in long longitudinal cracks in this region. Above Piers 108–109, more than 2 MPa longitudinal tensile stress distributes along the outer edge of the last cast pylon wall, resulting in multiple parallel vertical cracks in this region.

In addition, at the bottom of the pylon near Pier 110, more than 2 MPa shrinkage tensile stresses are generated because the shrinkage deformation of the concrete is constrained by the foundation.

4.3. Effect of Cable Force Reduction

In order to analyze the effect of cable force reduction on bridge mechanical performance, the deformations and stresses of the pylon and girder with design and measured cable force are compared.

With the design cable forces, the structural deformation under self-weight is shown in Figure 18a, and the deformation under self-weight and live load is shown in Figure 18b. The girder is arched upward by 64 mm and 46 mm, respectively. The vertical displacement (UY) at the pylon top ranges from −7 mm to −6 mm, the longitudinal displacement (UZ) is about 8 mm, and the pylon tips forward.
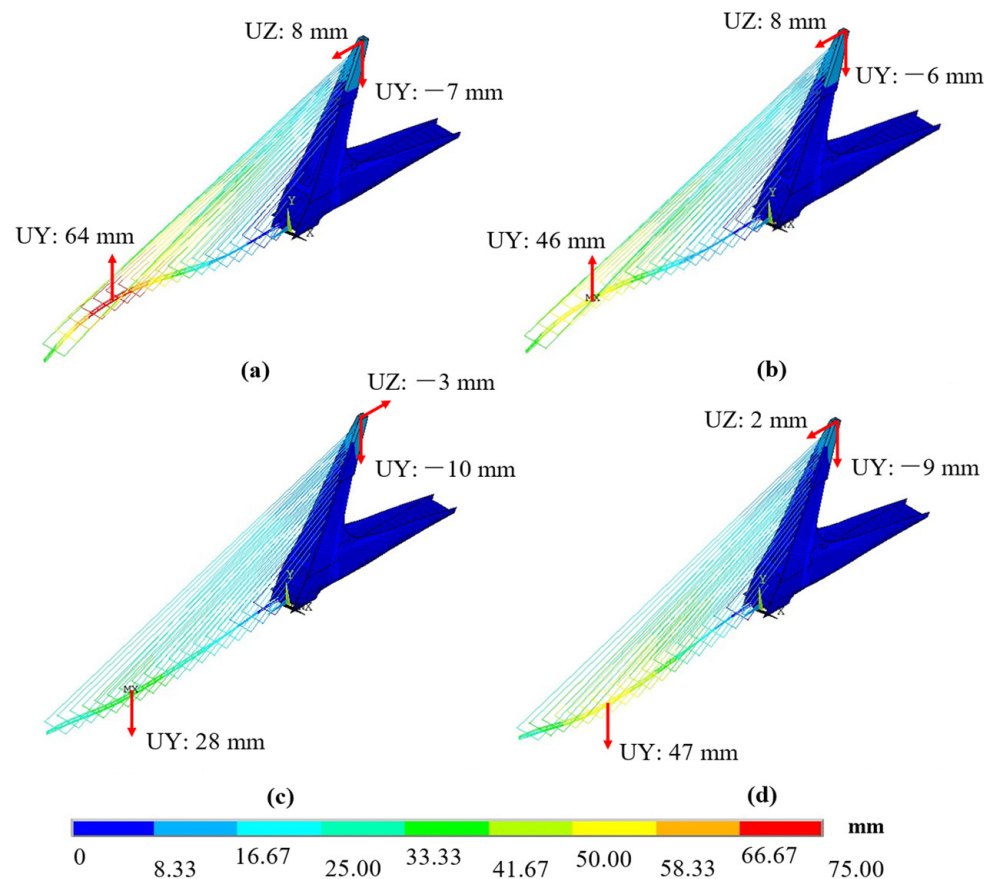

Figure 18. The deformation of pylon and girder with different cable forces: (**a**) design cable force self-weight; (**b**) design cable force self-weight and live load; (**c**) measured cable force self-weight; (**d**) measured cable force self-weight and live load.

With the measured cable force, the structural deformation under self-weight is shown in Figure 18c. The girder deflects downward by about 28 mm, UY at the pylon top is −10 mm, and UZ is −3 mm. The pylon tips backward due to the insufficient cable force. After loading the live load in the middle span of the girder, the cable force increases significantly, and the deformation of the pylon changes to a forward tilt, as shown in

Figure 18d. The girder deflects downward by about 47 mm, UY at the pylon top is −9 mm, and UZ is 2 mm.

The stress of the pylon under self-weight with different cable forces is shown in Figure 19. With design cable force, the pylon is generally compressed, with less than 1.5 MPa tensile stress distributing at the pylon top, the transverse joints of the pylon wall, and the anchorage area of the stayed cables.
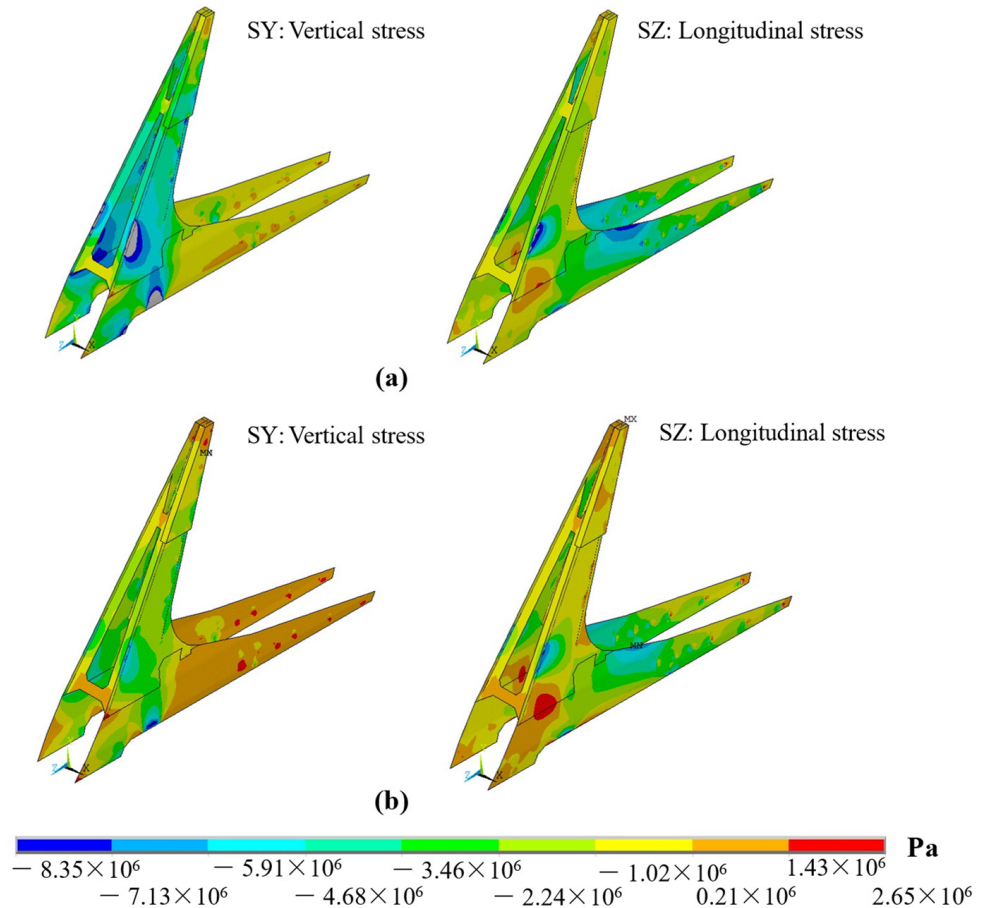

Figure 19. The stress of the pylon under self-weight with different cable forces: (**a**) stress of pylon under self-weight with design cable force; (**b**) stress of pylon under self-weight with measured cable force.

With measured cable force, the pylon tilts backward, creating a negative bending moment at the root of the pylon, resulting in a change from compression to tension in Region 3. About 1.5 MPa tensile stress occurs in Region 3. The distribution of tensile stress at the pylon top, the transverse joints, and the anchorage area of the stayed cables are enlarged.

4.4. Effect of Temperature Load

Under self-weight and temperature load, more than 1.5 MPa tensile stress is generated in Region 3, the transverse joints of the pylon wall, and the anchorage area of the stayed cables, as shown in Figure 20a.

Due to the restraining of the supports and foundations, the temperature load greatly affects Region 3, and more than 4 MPa longitudinal tensile stress is generated, as shown in Figure 20b.
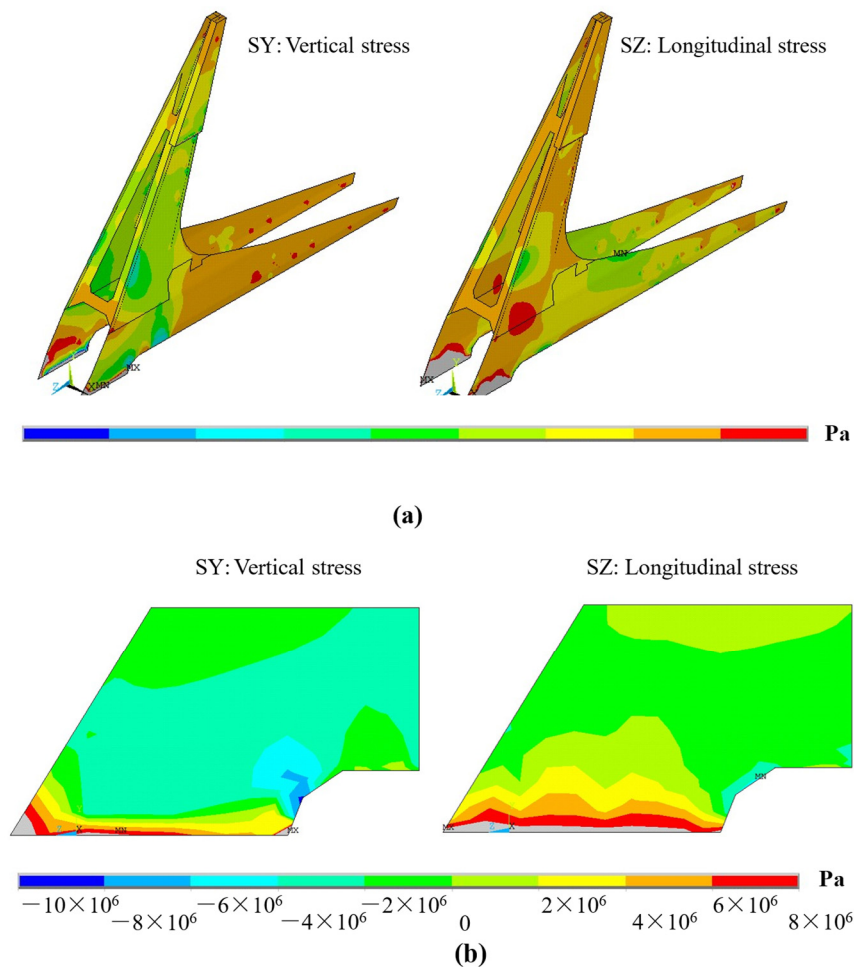
Figure 20. The stress of the pylon and Region 3 under self-weight and temperature load: (**a**) pylon; (**b**) Region 3.

5. Forensic Analysis of Damage

Based on the time-dependent FE analysis and comparisons of cracks between the investigation and the simulation results, the causes of the cracks in these three categories of the pylon are proposed below.

5.1. Crack Category L1

Crack Category L1 includes the longitudinal cracks at the bottom of the pylon, and the parallel vertical cracks distributed at the last casting pylon wall between Piers 108 and 109, as shown in Figure 21a. Figure 21b,c show the contour distribution of vertical and longitudinal tensile stress.

The gray and blue boxes in Figure 21a show the zones where there is a vertical or longitudinal tensile stress distribution of more than 2 MPa, which are the assumed cracking zones. The dimensions of the simulated cracking areas (black marks) were measured and compared with the lengths of the cracks (red marks) in this region. There are some differences between the lengths of calculated tensile zones and the lengths of the cracks, but most of the cracks are located within the calculated tensile zones.

Combining the results of construction process analysis and parameter comparison, the cause for the cracks in category L1 is attributed to the effect of concrete shrinkage. The shrinkage strain of the new concrete layer is restricted by the old one. Thus, a larger tensile stress occurs near the interface of the new and old concrete layers, which results in the concrete cracking. The construction process simulation results confirm that these cracks

appear at construction stage 1 and construction stage 8 and expand during the long-term shrinkage effect.
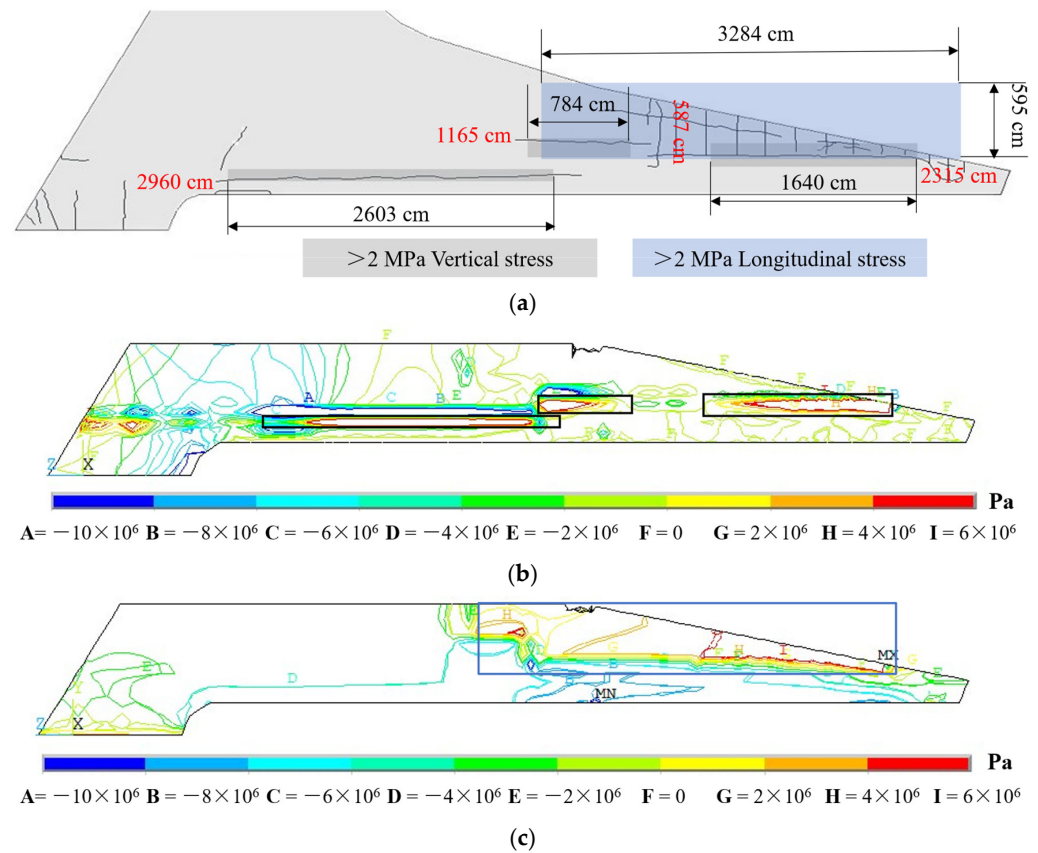

Figure 21. Distribution of Crack Category L1 and stress in Region 1: (**a**) distribution of cracks in Category L1; (**b**) contour distribution of vertical stress; (**c**) contour distribution of longitudinal stress.

5.2. Crack Category L2

Crack Category L2 includes the inclined cracks located in the anchorage region of cable 10 to cable 18. The direction of these cracks is almost parallel to the cables, as shown in Figure 22a. Figure 22b shows the distributions of the principal tensile stress. The direction of the stress is almost perpendicular to the cables.
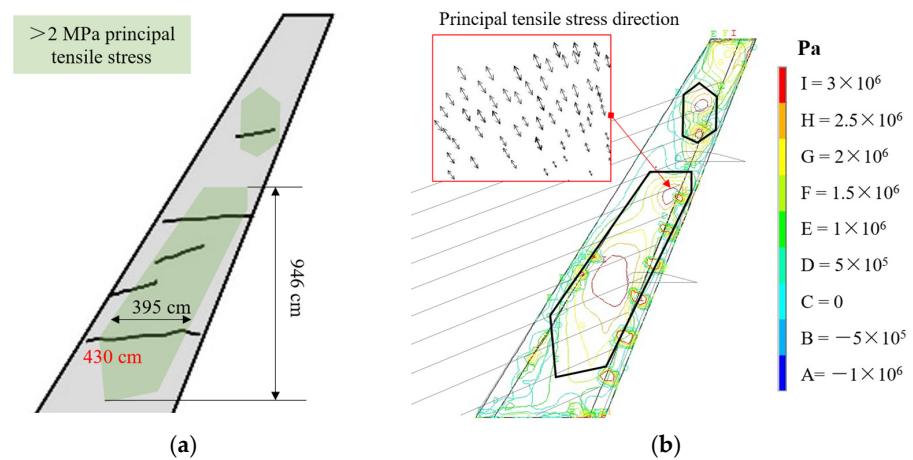

Figure 22. Distribution of Crack Category L2 and principal stress in Region 2: (**a**) distribution of cracks in Category L2; (**b**) contour distribution and direction of principal stress.

The green polygon boxes in Figure 22a show the zones where the principal tensile stress is more than 2 MPa, which are the assumed cracking zones. Most of the diagonal cracks in Region 2 are within the calculated tension zones.

The principal tensile stress in Region 2 is caused by many factors: (1) The tensile stress perpendicular to the cables could occur around the anchorage region due to the Poisson effect. (2) There is an angle between the direction of cables and the longitudinal bridge direction. The cable force generates a component force F_x directed toward the outside of the pylon, as shown in Figure 23, which further results in an out-of-plane bending moment to the pylon. The tensile stress thus occurs around the outside of the pylon. (3) The anchorage of the prestressed tendons in the pylon exacerbates the complexity of the forces in this region.
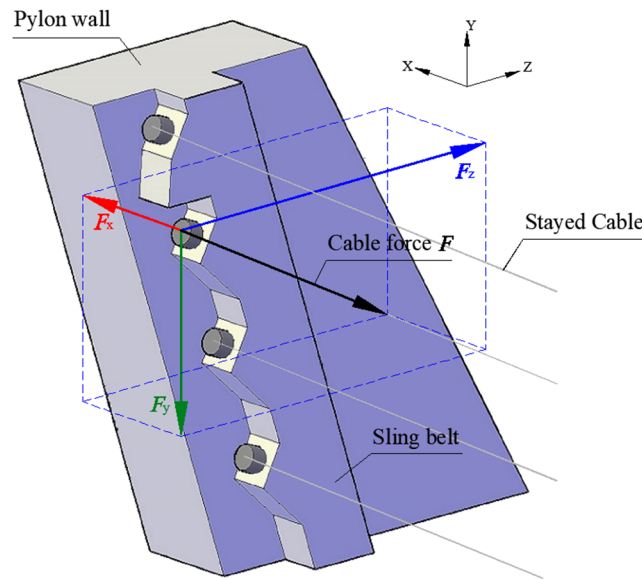

Figure 23. Structure and force diagram of anchorage region of cables.

5.3. Crack Category L3

Crack Category L3 includes short vertical and longitudinal cracks located in Region 3, as shown in Figure 24a. Figure 24b,c show the distribution of vertical and longitudinal stresses. The gray and blue boxes in Figure 24a show the zones where the vertical or longitudinal tensile stress is more than 2 MPa, which are the assumed cracking zones. The crack distribution agrees well with the tensile stress distribution.
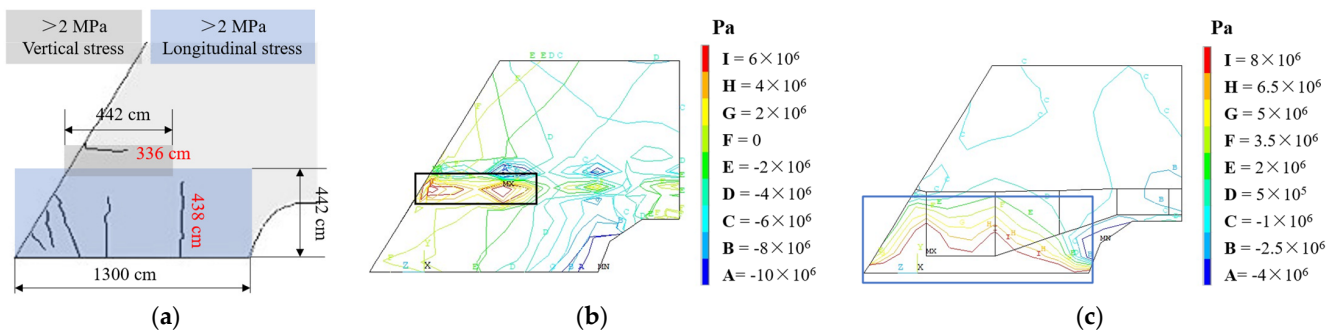

Figure 24. Distribution of Crack Category L3 and stress in Region 3: (**a**) distribution of cracks in Category L3; (**b**) contour distribution of vertical stress; (**c**) contour distribution of longitudinal stress.

Multiple causes create the tensile stress in Region 3. The vertical tensile stress caused by concrete shrinkage results in short longitudinal cracks in this region. The combination of longitudinal tensile stress generated by temperature load and concrete shrinkage results

in vertical cracks at the bottom of the pylon. In addition, due to the reduction in cable force, especially the cables of C10~C18 (see Figure 6), the pylon tilts backward during service, which results in a large negative bending moment at the root of the pylon, exacerbating the cracking in Region 3.

6. Conclusions

This paper uses the BIM model and FE analysis method to conduct the damage forensic analysis of a cable-stayed bridge without backstays. The BIM model is established based on the recorded design and construction information. Then, the FE model for different construction stages is generated based on the BIM model. After that, the causes for the severe cracking in the pylon are carefully analyzed and revealed. The major conclusions are as follows:

(1)   A large difference in concrete age and shrinkage exists in the pylon due to the unreasonable process of concrete casting in construction, which results in longitudinal and vertical cracks in the pylon walls between Piers 108 and 109.

(2)   The Poisson effect and the component of the cable force lead to incline cracks in the anchorage zone of C10~C18 cables. Moreover, the unsuitable positions of the anchorage of the prestressed tendons in the pylon exacerbate the development of cracks in the region.

(3)   The combination of temperature load and shrinkage results in short vertical and longitudinal cracks in the pylon near Pier 110. The measured force of stayed cables is less than the corresponding design force, which results in a negative bending moment at the bottom of the pylon, exacerbating the cracking.

(4)   The cause of cracks in the bridge is closely related to the shrinkage effect of the mass concrete bridge pylon cast in stages. It is necessary to carry out the construction process simulation and crack resistance analysis during the design.

(5)   The combined analyses using the BIM and FE methods agree well with the field inspection and provide a better way to reveal and understand the causes and distribution of cracks.

Author Contributions: Conceptualization, Q.X., X.S. and H.M.; methodology, Q.X., X.S. and Z.X.; investigation, Q.X. and Z.X.; writing—original draft preparation, Q.X. and H.M.; writing—review and editing, Z.X. and X.S.; supervision, X.S. and H.M.; funding acquisition, X.S. and H.M. All authors have read and agreed to the published version of the manuscript.

Institutional Review Board Statement: Not applicable.

Informed Consent Statement: Not applicable.

Data Availability Statement: The original contributions presented in the study are included in the article, further inquiries can be directed to the corresponding author.

Conflicts of Interest: The authors declare no conflicts of interest.

References

1.   Virlogeux, M. Recent Evolution of Cable-stayed Bridges. *Eng. Struct.* **1999**, *21*, 737–755. [CrossRef]
2.   Pollalis, S.N. *What Is a Bridge? The Making of Calatrava's Bridge in Seville*; The MIT Press: Cambridge, MA, USA, 1999; pp. 2–16.
3.   Gimsing, N.J.; Georgakis, C.T. *Cable Supported Bridges: Concept and Design*; John Wiley & Sons: Hoboken, NJ, USA, 2011.
4.   Kominek, M. The Marian Bridge, Czech Republic. *Struct. Eng. Int.* **1998**, *8*, 283–284. [CrossRef]
5.   Shao, X.D.; Zhao, H.; Li, L.F. Design and Experimental Study of a Harp Shaped Single Span Cable-stayed Bridge. *J. Bridge Eng.* **2005**, *10*, 658–665. [CrossRef]

6. Peng, W.H.; Shao, X.D.; Li, L.F. The Concept, Design, and Construction of Cable-stayed Bridges without Backstays. *China Civ. Eng. J.* **2007**, *5*, 26–33.

7. Chen, D.W.; Au, F.T.K.; Tham, L.G.; Lee, P.K.K. Determination of Initial Cable Forces in Prestressed Concrete Cable-stayed Bridges for Given Design Deck Profiles Using the Force Equilibrium Method. *Comput. Struct.* **2000**, *74*, 1–9. [CrossRef]

8. Chen, A.J.; He, G.J. Analysis on Reasonable Structure of Main Girder of Harp Shaped Cable-stayed Bridge without Backstays. *Appl. Mech. Mater.* **2011**, *90–93*, 1061–1068. [CrossRef]

9. Wu, Y.; Li, J.; Sun, Q. Study on Human-induced Vibration of a Cable-stayed Bridge without Backstays Located in Abrupt Valley. *Adv. Struct. Eng.* **2021**, *24*, 3101–3117. [CrossRef]

10. Wu, Y.; Wu, X.; Li, J.; Xin, H.; Sun, Q.; Wang, J. Investigation of Vortex-induced Vibration of a Cable-stayed Bridge without Backstays Based on Wind Tunnel Tests. *Eng. Struct.* **2022**, *250*, 113436. [CrossRef]

11. Kang, H.J.; Qian, D.Y.; Su, X.Y.; Zhang, X.Y.; Cong, Y.Y. A New Technique for Calculating the Effective Length Factor of the Tower in Cable-Stayed Bridge. *Int. J. Struct. Stab. Dyn.* **2023**, *23*, 2350130. [CrossRef]

12. Zhang, Q.C.; Sun, Q.S. Analysis of Parameter Sensitivity in Construction Control of Inclined Pylon Cable-Stayed Bridge without Backstays. *Adv. Mater. Res.* **2011**, *255–260*, 851–855. [CrossRef]

13. Antonio Lozano-Galant, J.; Turmo, J. Creep and Shrinkage Effects in Service Stresses of Concrete Cable-stayed Bridges. *Comput. Concr.* **2014**, *13*, 483–499. [CrossRef]

14. Duan, H.; Liu, H.; Sun, Y.; Gao, H.S. Determination of Reasonable Internal Force State for Cable-stayed Bridge without Backstays. *J. Civ. Struct. Health Monit.* **2023**, *13*, 1243–1263. [CrossRef]

15. Ratay, R.T.; Peraza, D.B. Investigation and Analysis of Structural Collapse. *Encycl. Forensic Sci.* **2013**, *2*, 461–465.

16. Saeed, M.K.; Rahman, M.K.; Baluch, M.H.; Tooti, L.A. Cracking in Concrete Water Tank due to Restrained Shrinkage and Heat of Hydration: Field Investigations and 3d Finite Element Simulation. *J. Perform. Constr. Facil.* **2020**, *34*, 04019100. [CrossRef]

17. Etemadi, A.; Balkaya, C. Collapsed-RC Building Failure Mechanisms with a Forensic Engineering Approach. *J. Perform. Constr. Facil.* **2020**, *33*, 04020086. [CrossRef]

18. Cuoco, D.A.; Scarangello, T.Z.; Peraza, D.B. Investigation of L'Ambiance Plaza Building collapse. *J. Perform. Constr. Facil.* **1992**, *6*, 211–231. [CrossRef]

19. Delatte, N.J. *Beyond Failure*; ASCE: Reston, VA, USA, 2007.

20. Brando, F.; Iannitelli, A.; Cao, L.; Malsch, E.A.; Panariello, G.; Abruzzo, J.; Pinto, M.J. Forensic Investigation Modeling (FIM) Approach: I35 West Bridge Collapse Case Study. In Proceedings of the Forensic Engineering 2012: Gateway to a Safer Tomorrow, San Francisco, CA, USA, 31 October 2012.

21. Campione, G.; Giambanco, G. Analysis of a Collapsed Long span Reinforced Concrete Roof in South Italy: Design Mistakes and Material Degradation. *J. Perform. Constr. Facil.* **2020**, *34*, 04020001. [CrossRef]

22. Palmisano, F.; Vitone, A.; Vitone, C.; Vitone, V. Collapse of the Giotto Avenue Building in Foggia. *Struct. Eng. Int.* **2007**, *17*, 166–171. [CrossRef]

23. Palmisano, F.; Vitone, A. Partial Collapse of One of the Most Important Historical Building in Salerno, Italy. *J. Perform. Constr. Facil.* **2015**, *29*, 04014164. [CrossRef]

24. Korkmaz, H.H.; Yakut, A.; Bayraktar, A. Analysis of a Multistory Reinforced Concrete Residential Building Damaged under Its Self Weight. *Eng. Fail. Anal.* **2019**, *98*, 38–48. [CrossRef]

25. Balkaya, C. Lessons Learned from Collapse of Zumrut Building under Gravity Loads. *Int. J. Eng. Technol.* **2017**, *3*, 44–49. [CrossRef]

26. Park, J.; Cai, H.; Dunston, P.S.; Ghasemkhani, H. Database-supported and Web-based Visualization for Daily 4D BIM. *J. Constr. Eng. Manag.* **2017**, *143*, 04017078. [CrossRef]

27. Hu, Z.; Zhang, J. BIM-and 4D-based Integrated Solution of Analysis and Management for Conflicts and Structural Safety Problems during Construction: 2. Development and Site Trials. *Autom. Constr.* **2011**, *20*, 167–180. [CrossRef]

28. Mcguire, B.; Atadero, R.; Clevenger, C.; Ozbek, M. Bridge information modeling for inspection and evaluation. *J. Bridge Eng.* **2016**, *21*, 04015076. [CrossRef]

29. Kim, S.; Ma, J.; Lee, J.; Hong, T.; An, J.; Jeong, K. Framework of BIM-Based Quantitative Evaluation for Enhancing Fire Safety Performance of Buildings. *J. Manag. Eng.* **2024**, *40*, 04023061. [CrossRef]

30. Levine, N.M.; Spencer, B.F., Jr. Post-Earthquake Building Evaluation Using UAVs: A BIM-Based Digital Twin Framework. *Sensors* **2022**, *22*, 873. [CrossRef]

31. *Computer Software*, Version 15.0; ANSYS Release 15.0; ANSYS, Inc.: Canonsburg, PA, USA, 2015.

32. ANSYS, Inc. *ANSYS Manual*; ANSYS, Inc.: Canonsburg, PA, USA, 2015.

33. *JTG 3362-2018*; Ministry of Communications and Transport (MOCAT). Specifications for Design of Highway Reinforced Concrete and Prestressed Concrete Bridges and Culverts. China Communications Press: Beijing, China, 2018.

34. *JTG D60-2015*; Ministry of Communications and Transport (MOCAT). General Specifications for Design of Highway Bridges and Culverts. China Communications Press: Beijing, China, 2015.